Interfacial Manipulation via In-Situ Grown ZnSe Overlayer toward Highly Reversible Zn Metal Anodes

Xianzhong Yang
Soochow University
Chao Li
Shandong University of Technology
Zhongti Sun
Soochow University
Shuai Yang
State Key Laboratory of Low Dimensional Quantum Physics, Department of Physics, Tsinghua University
Zixiong Shi
Soochow University
Rong Huang
Soochow University
Bingzhi Liu
Soochow University
Shuo Li
Soochow University
Yuhan Wu
Soochow University
Menglei Wang
Soochow University
Yiwen Su
Soochow University
Shi Xue Dou
University of Wollongong https://orcid.org/0000-0003-3824-7693
Jingyu Sun (sunjy86@suda.edu.cn)
Soochow University

Article

Keywords: Zn metal anode, Energy storage, Batteries, energy and catalysis

Posted Date: April 20th, 2021

DOI: https://doi.org/10.21203/rs.3.rs-400312/v1

Abstract

Zn metal anode has garnered growing scientific and industrial interest owing to its appropriate redox potential, low cost and good safety. Nevertheless, the instability of Zn metal, caused by dendrite formation, hydrogen evolution and side reactions, gives rise to poor electrochemical stability and unsatisfactory cycling life, greatly hampering large-scale utilization. Herein, an *in-situ* grown ZnSe layer with controllable thickness is crafted over one side of commercial Zn foil *via* chemical vapor deposition, aiming to achieve optimized interfacial manipulation between aqueous electrolyte/Zn anode. Thus-derived ZnSe overlayer not only prevents water penetration and restricts Zn^{2+} two-dimensional diffusion, but also homogenizes the electric field at the interface and facilitates favorable (002) plane growth of Zn. As a result, dendrite-free and homogeneous Zn deposition is obtained; side reactions are concurrently inhibited. In consequence, a high Coulombic efficiency of 99.2% and high cyclic stability for 860 cycles at 1.0 mA cm^{-2} in symmetrical cells is harvested. Meanwhile, when paired with V_2O_5 cathode, assembled full cell achieves an outstanding initial capacity (200 mAh g^{-1}) and elongated lifespan (a capacity retention of 84% after 1000 cycles) at 5.0 A g^{-1}. Our highly reversible Zn anode enabled by the interfacial manipulation strategy is anticipated to satisfy the demand of industrial and commercial use.

Introduction

Recent years have witnessed a burgeoning development of advanced energy storage systems to meet the urgent energy demand in individual and industrial applications. In this sense, aqueous rechargeable batteries have stimulated increased attentions due to their intrinsic safety and environmental benignity, as compared to their counterparts with flammable organic electrolytes[1–4]. The high ionic conductivity of aqueous electrolyte in addition endows the corresponding devices with excellent rate performance and fast reaction kinetics. To capitalize on these merits, aqueous Zn-ion batteries (AZIBs) coupled with affordable and nontoxic features are worthy of in-depth investigation. More encouragingly, Zn metal is an appealing anode candidate on the ground of outstanding volumetric specific capacity (5855 mAh cm^{-3}) and appropriate redox potential (− 0.76 V *vs*. standard hydrogen electrode)[5, 6]. Nevertheless, the commercial Zn foil anode is far from ideal to realize reversible dissolution/deposition during electrochemical cycling (Scheme 1a). This is primarily owing to the fact that the surface protuberance is highly likely to trigger an intense cusp effect, in turn resulting in the uneven deposition of Zn and radical formation of dendrites[7, 8]. Thus-grown dendrites could ultimately pierce the separator and induce short-circuit failure of the battery[9]. Meanwhile, problematic issues including hydrogen evolution[10] and side reactions[11] remain urgent to be solved since they are main origins of catastrophic volume expansion, electrode corrosion and surface passivation. Therefore, it is of vital importance to develop effective avenues to protect Zn anode from these caveats toward the realization of high-performance AZIB devices.

In response, strategic efforts have been devoted to tackle aforementioned bottlenecks in pursuit of achieving highly reversible Zn anodes[2], which mainly encompass electrolyte modulation[12–14], host

design[15] and interface engineering[16]. Firstly, the composition and concentration of electrolytes exert a significant impact on the Zn stripping/plating behaviors. For instance, the innovative “water in salt” electrolyte (1 M $Zn(TFSI)_2$ and 20 M LiTFSI) can effectively restrain Zn dendrite and suppress hydrogen evolution throughout forming a new solvation sheath[13]. Secondly, zincophilic host design allows the dictation of the Zn/host interface to harvest a low Zn nucleation barrier[15] or facilitate a heteroepitaxial Zn nucleation[17], accordingly enabling the inhibition of the dendrite growth. Last but not the least, Zn/electrolyte interface engineering has been extensively explored due to its direct influence over Zn nucleation and growth. This can be implemented by introducing artificial protective layer comprising conductive or non-conductive coatings[11]. The conductive coatings, such as graphene[4], MXene[16], In[18], Au[19] and Cu[20], are beneficial to guiding a homogeneous Zn deposition to eliminate the dendrite. In parallel, the non-conductive shields, including TiO_2[21, 22], $CaCO_3$[23], ZnO[24], ZrO_2[25], ZnS[26] and kaolin[27], would deactivate the dendritic formation *via* decreasing the nucleation energy barrier and inhibit hydrogen evolution by protecting the active Zn from the direct attack of the bulk electrolyte. Despite promising protection effects achieved on the anode side, it is worth noting that these prevailing strategies rely heavily upon *ex-situ* coating of foreign layers over Zn foils, which normally leads to non-uniform films with uncontrolled thickness uniformity and limited production scalability. In turn, the high-rate cyclability could be disabled and the energy density of entire device might be undermined. This would ultimately spur us to develop a simple yet effective method to precisely regulate the anode/electrolyte interface toward stabilized Zn anode.

Herein, we devise a highly reversible Zn anode realized by *in-situ* grown Zn selenide (ZnSe) overlayer *via* chemical vapor deposition (CVD) (Scheme 1b), accomplishing efficient interface manipulation in a manner analogous to the artificial solid electrolyte interphase (SEI) for alkali metal anode protection[28]. Our designing strategy harnessing sufficient scalability and intrinsic simplicity holds the potential to adequately meet practical demands. The initially disordered Zn protuberances are converted to ZnSe nanoparticles upon selenization, where ultrathin ZnSe layer is accordingly produced and uniformly bound to Zn metal to form a vertically aligned heterostructure (ZnSe@Zn). Such an interface engineering can simultaneously lower the Zn nucleation overpotential and homogenize the local current density to a great extent. The favorable zincophilicity of ZnSe would help restrict the two-dimensional diffusion of Zn ions along the interface. As a result, the growth of Zn dendrite is effectively inhibited. In addition, the *in-situ* formed ZnSe overlayer enables to decline the de-solvation energy barrier of hydrated-Zn, thereby boosting Zn^{2+} transfer kinetics and deactivating hydrogen evolution. Benefiting from our interfacial manipulation, thus-derived ZnSe@Zn anode features an elongated lifespan of 860 h at a current density of 1.0 mA cm^{-2}. It can even sustain a stable stripping/plating operation at 10 mA cm^{-2} for as long as 260 h. More impressively, the full cell based on ZnSe@Zn anode harvests a capacity retention of 84% after 1000 cycles at 5.0 A g^{-1}. Our highly reversible Zn anode enabled by the interfacial manipulation strategy is anticipated to satisfy the demand of industrial and commercial use.

Results

Synthesis and characterization of ZnSe overlayer.

Fig. 1a schematically depicts the synthetic set-up for the *in-situ* growth of ZnSe overlayer on commercial Zn foil by CVD. The Zn foil serving as the growth substrate is placed at the downstream of the Ar/H_2 gas flow, which assists to carry the sublimed Se powders coming from the upstream (See Methods). This ambient-pressure process is facile, simple, economical and potentially scalable. It also bypasses the lengthy high-temperature annealing and tedious vacuum operations. The size of the product, ZnSe@Zn, is merely limited by the furnace dimension. Fig. 1b presents a digital photograph of a 20 cm × 10 cm sized ZnSe@Zn foil with perfect film homogeneity produced in a 4-inch tube furnace, demonstrating the viability of large-scale synthesis toward practical applications. The surface morphology of ZnSe overlayer was examined by scanning electron microscopy (SEM) and atomic force microscopy (AFM). As shown in Fig. 1c, the full coverage of ZnSe layer upon CVD reaction is helpful to even out a plethora of sharp protuberances on bare Zn surface (Supplementary Fig. 1). Close-up view further suggests that thus-grown ZnSe exists in the form of nanoparticles with diameters of 30-50 nm (Fig. 1c inset; Supplementary Fig. 2). Such a three-dimensional porous texture would be beneficial to Zn^{2+} transport. Notably, the thickness of ZnSe overlayer can be simply dictated by controlling the CVD synthetic parameters, *i.e.*, altering the temperature ramping rate and dwelling duration (Fig. 1d; Supplementary Fig. 3). Fig. 1e presents a side-view SEM image of ZnSe overlayer (affording a thickness of 0.75 μm), where corresponding elemental maps manifest uniform distribution of detected elements.

The wettability to electrolyte is one of the key factors for reversible Zn stripping/plating as it exerts influence upon interfacial ion-transfer resistance[8]. In this respect, bare Zn foil possesses a fairly poor wettability by 2 M $ZnSO_4$ electrolyte, displaying a contact angle of 82° based on static contact angle measurement (Fig. 1f). In contrast, the contact angle sharply declines to 14° on ZnSe@Zn foil (ZnSe thickness: 0.75 μm), implying markedly enhanced wettability (Fig. 1g). The contact angle values in the case of ZnSe@Zn foil with different ZnSe thickness are further compared (Supplementary Fig. 4), amongst which the 0.75 μm-thick ZnSe harvests the smallest contact angle. Collected XRD patterns of ZnSe@Zn and bare Zn indicate that the ZnSe grows primarily along (111) direction (Fig. 1h; Supplementary Fig. 5)[29]. Recognizable Raman signals further verify the successful preparation of ZnSe overlayer (Supplementary Fig. 6).

Electrochemical performance of ZnSe@Zn

To evaluate the plating/stripping reversibility and Zn utilization of Zn anode with/without ZnSe protection, Coulombic efficiency (CE) measurements were carried out in two-electrode cells (ZnSe@Ti–Zn and Ti–Zn) with a fixed capacity of 0.5 mAh cm^{-2} at a current density of 2.0 mA cm^{-2}. The ZnSe coating on Ti foil was obtained by CVD to derive the ZnSe@Ti electrode (Supplementary Fig. 7). In terms of the galvanostatic cycling performance, ZnSe@Ti–Zn cell presents an initial plating-stripping voltage hysteresis of 87 mV, which is obviously lower than that (133 mV) of bare Ti–Zn cell (Fig. 2a inset; Supplementary Fig. 8). Encouragingly, ZnSe@Ti–Zn cell could maintain 400 cycles with an average CE of 99.2%, indicating favorable reversibility and excellent durability (Fig. 2a). In stark contrast, bare Ti–Zn cell

merely sustains for 50 cycles with drastic fluctuations of CE values, suggesting the presence of side reactions and dendrite growth. It is safe to conclude that the ZnSe overlayer would well manipulate the nucleation and growth of Zn toward a highly reversible anode.

To verify the advanced effect of anode protection *via in-situ* formed ZnSe overlayer, galvanostatic cyclic stability of symmetric cells was evaluated under various current densities and areal capacities. Fig. 2b shows the long-term cycling performance of bare Zn and ZnSe@Zn symmetric cells at 1.0 mA cm^{-2} with a capacity of 1.0 mAh cm^{-2}. Upon cycling for ~80 h, a sudden and irreversible voltage rise occurs for bare Zn cell, which could be attributed to the accumulation of adverse “dead Zn” and by-products. The presence of these species is detrimental throughout occluding ion transport pathways, resulting in a large voltage hysteresis of 128 mV. In contrast, ZnSe@Zn symmetric cell readily displays a far more stable voltage profile with much declined voltage hysteresis of 30 mV that sustains more than 860 h, approximately 10 times longer in comparison with bare Zn cell. Note that our CVD route is versatile enough to enable the delicate control over the thickness of ZnSe layer, where an optimized thickness at 0.75 μm could be gained in response to generating the smallest polarization (Supplementary Fig. 9). This result echoes well with the observation from electrolyte wettability tests. The refinement of electrolyte/ZnSe@Zn interface, which expedites the electrokinetics of Zn deposition, can further be confirmed throughout electrochemical impedance spectroscopy (EIS) analysis. As disclosed in the Nyquist plots in Fig. 2c, the impedance of the bare Zn cell manifests a remarkable increase (from 0.7 to 7.7 kΩ) after 10 cycles, whereas the impedance of the ZnSe@Zn cell shows a slight decrease from 0.4 to 0.25 kΩ, revealing that the ZnSe overlayer is competent in declining charge transfer resistance in aqueous $ZnSO_4$ electrolyte. According to Sand’s model[30], the formation time of dendrite is inversely proportional to current density. In addition, the interfacial electric field becomes rather uneven under elevated current densities, inducing less yet adverse nucleation sites. Areal specific capacity is also a nontrivial factor, where a higher one would augment the dendrite size. Therefore, Zn plating/stripping behavior quickly deteriorates under high current densities/capacities due to rampant dendrite formation[7]. Impressively, the ZnSe@Zn cell still remains highly stable for more than 250 h even under the high current density/capacity at 10.0 mA cm^{-2}/10.0 mAh cm^{-2} (Fig. 2d; Supplementary Fig. 10), representing one of the best performances achieved by far in such stringent conditions (Supplementary Table 1). Fig. 2e displays the rate performances of symmetric cells with a fixed capacity of 1.0 mAh cm^{-2} under varied current densities from 1.0 to 10.0 mA cm^{-2}. Apparently, ZnSe@Zn cell harvests a much lower voltage hysteresis at all current densities in comparison with bare Zn counterpart, demonstrating superior stability and high reversibility. In addition, dramatic reduction of nucleation overpotential tested under various conditions was witnessed upon the introduction of ZnSe overlayer (Supplementary Fig. 11), which is conducive to uniform deposition of Zn.

Mechanism analysis on ZnSe protection effect

To probe the electrochemical protection mechanism of ZnSe overlayer in $ZnSO_4$ electrolyte system, *in-situ*/*ex-situ* scrutinization in combination with electroanalytic characterization were carried out. First of

all, real-time Zn plating/stripping process in transparent cell configuration was visualized with the aid of *operando* optical microscopy. A current density of 5.0 mA cm^{-2} was employed for the electrodeposition. As depicted in Fig. 3a, a number of randomly distributed protrusions commence to appear on the surface of bare Zn anode after 30 min deposition. When the deposition time reaches 60 min, the growth of dendrites is evident. In comparison, ZnSe@Zn anode retains a smooth surface texture during the entire plating process with no discernible dendritic formation (Fig. 3b), intuitively reflecting the capability of ZnSe overlayer in restraining the dendrite growth. Post-mortem SEM characterization of bare Zn and ZnSe@Zn anodes in transparent cells was conducted after 40-cycled plating/stripping process at 1.0 mA cm^{-2} (Fig. 3c-f; Supplementary Fig. 12). As for the bare Zn anode, along with the mossy Zn generated on the surface, noticeable pits (marked by dotted cycle in Fig. 3c) are also produced owing to the uneven plating/stripping and severe side reactions[31, 32]. By contrast, the ZnSe@Zn anode affords a compact, uniform and dendrite-free morphology with no observed protuberances and/or pits (Fig. 3e). Moreover, the thickness of deposited Zn on ZnSe@Zn anode (15 μm) stays much smaller as compared to that on bare Zn (136 μm), indicative of effective mitigation of dendrite formation with the ZnSe overlayer. Supplementary results for electrodes cycled at 5.0 mA cm^{-2} in transparent cells and at 1.0 mA cm^{-2} in coin cells further corroborate the positive impact of ZnSe protection (Supplementary Fig. 13 and 14).

Post-mortem XRD was performed to identify the composition change of cycled electrodes. As shown in Fig. 3g, $Zn_4SO_4(OH)_6.4H_2O$ by-product is proven to be generated on bare Zn upon cycling. This insoluble species would inevitably induce high overpotential of Zn symmetric cell due to its impenetrable nature for Zn ion. In contrast, there is no trace of by-product diffraction peak for ZnSe@Zn electrode, implying high reversibility of Zn dissolution/deposition reaction by virtue of ZnSe overlayer. Note further that the peak intensity ratio of Zn (002) to Zn (101) plane for ZnSe@Zn after cycling significantly augments about 12 times as compared to that for bare Zn. The existing similarity of lattice structure between ZnSe (111) and Zn (002) plane possibly guide an oriented Zn formation (Supplementary Fig. 15 and 16), where ZnSe layer can act as a template to induce (002) monocrystal Zn. Such a Zn growth behavior is desirable for anode protection[17, 33]. More intriguingly, there is no sign of ZnSe signals whatsoever for the ZnSe@Zn electrode after cycling, indicating the fall-off of ZnSe coating from the Zn foil, in good agreement with visualized characterizations (Supplementary Fig. 16; Supplementary Video 1). This phenomenon stems primarily from the fact that Zn is deposited at the interface between ZnSe overlayer and underlying Zn foil, where a flat and oriented Zn film is readily formed prior to the ZnSe detachment. Thus-produced Zn film enables to continuously guide a uniform Zn deposition even in the absence of ZnSe coating. Collectively, our results demonstrate that ZnSe overlayer is crucial to achieve optimized interfacial manipulation targeting highly reversible Zn anode.

The suppression effect on Zn corrosion *via* ZnSe overlayer was analyzed by linear polarization tests in 2 M $ZnSO_4$ electrolyte (Fig. 3h). In comparison with bare Zn, the corrosion potential of the ZnSe@Zn reaches −1.013 V (−1.017 V for bare Zn), suggesting that it is less prone to corrosion. Meanwhile, the declined corrosion current by *ca.* 300 μA cm^{-2} again represents a retarded corrosion rate[34]. It is well received that the corrosion mainly originates from hydrogen evolution reaction (HER) accompanied by Zn

dissolution/deposition reaction in weakly acidic $ZnSO_4$ electrolyte[11]. Along this line, HER activity was additionally evaluated by linear sweep voltammetry (LSV) measurements[24]. As displayed in Fig. 3i, it is striking to find that ZnSe@Zn electrode harvests a depressed HER capability as compared to that of bare Zn electrode.

The solvation of Zn^{2+} is a major obstacle for circumventing rapid transport of Zn ions throughout the interface between electrolyte and Zn anode[24, 35]. The activation energy (E_a), which represents the energy required for de-solvation[36], can be quantitatively derived using the Arrhenius equation: $1/R_{ct} = A\exp(-E_a/RT)$, where R_{ct} is the charge transfer resistance and R is the ideal gas constant. Herein, R_{ct} (Supplementary Table 2) was fitted based on the variable-temperature EIS curves of Zn-Zn and ZnSe@Zn-ZnSe@Zn symmetric cells from 15 to 60 °C (Fig. 3j-k). It is evident that all R_{ct} values of ZnSe@Zn cell (Fig. 3k) are much lower than those of bare Zn cell (Fig. 3j). Accordingly, E_a of ZnSe@Zn can be calculated to be ~44.0 kJ mol^{-1} (Fig. 3l), in contrast to that of bare Zn cell (~67.5 kJ mol^{-1}). This result implies the superior kinetics of Zn^{2+} transfer throughout the interface between electrolyte and anode.

The nucleation and deposition of Zn relies heavily upon the electric field distributions at the anode/electrolyte interface[7, 16]. To investigate the role of *in-situ* grown ZnSe overlayer played in regulating interfacial electric field, finite element method carried out by COMSOL Multiphysics was employed. As depicted in Fig. 4a, the electric field distribution is homogeneous on bare Zn anode harnessing an ideally smooth surface. Nevertheless, the presence of micro-protrusions would strengthen the surrounding field intensity, which is expected to guide uneven deposition of Zn and lead to the dendrite formation (Fig. 4b). Encouragingly, these protuberances could be well eliminated by *in-situ* selenation process. In response, the peak value of field intensity sharply decreases from 2.2×10^5 to 1.6×10^4 V m^{-1} with the aid of ZnSe overlayer (Fig. 4c). Such a textured ZnSe coating further helps homogenize the electric field on Zn surface, followed by building up uniform charge flux.

Theoretical simulation based on density functional theory (DFT) route was performed to gain insight into the interaction between Zn and ZnSe. The calculated adsorption energy of a Zn atom on ZnSe support is apparently higher than that on bare Zn support (Fig. 4d; Supplementary Fig. 17). The strong affinity of Zn with ZnSe would be of benefit to suppressing two-dimensional (2D) diffusion of Zn ions. Chronoamperometry was accordingly employed to probe the Zn^{2+} diffusion dynamics at the anode/electrolyte interface (Supplementary Fig. 18). The current density of bare Zn symmetric cell continues to increase beyond 140 s under 150 mV, implying a violent 2D diffusion process. In turn, Zn^{2+} and hydrated Zn^{2+} ions tend to aggregate and grow into dendrites to minimize the surface energy (Fig. 4e). As for the ZnSe@Zn electrode, the 2D diffusion only occurs within the initial 20 s, after which a stable three-dimensional (3D) diffusion pattern becomes predominant. As illustrated in Fig. 4f, a desolvation process proceeds rapidly for hydrated Zn^{2+} ions upon their arrival at the ZnSe layer owing to low activation energy. Benefiting from a favorable 3D diffusion, Zn^{2+} could then pass through the ZnSe layer rapidly under the potential gradient resulting from the high electron resistance of ZnSe[37]

(Supplementary Fig. 19). This fast 3D diffusion process was confirmed by the high ionic conductivity of ZnSe layer reaching ~1.7×10^{-5} S cm^{-1} (Supplementary Fig. 20). Finally, these Zn ions are reduced to Zn^0 and start to grow along (002) plane on Zn metallic surface.

Electrochemical performance of AZIB full cells

To demonstrate the feasibility of thus-designed ZnSe@Zn anode in practical devices, AZIB full cells comprising $KV_{12}O_{30-y}{\cdot}nH_2O$ (KVOH)[38] cathode (see methods) and ZnSe@Zn anode were assembled employing 2 M $ZnSO_4$ electrolyte (Supplementary Fig. 21). Fig. 5a records the CV profiles of ZnSe@Zn–KVOH and bare Zn–KVOH cells at a scan rate of 0.1 mV s^{-1} in a voltage window between 0.2 and 1.6 V. Both cells manifest two main pairs of redox signals corresponding to two-step redox reactions of V^{3+}/V^{4+} and V^{4+}/V^{5+}. The higher current response of full cell with ZnSe@Zn anode as compared to bare Zn anode implies a higher capacity value, which can be confirmed by galvanostatic charge/discharge (GCD) curves in Fig. 5b. Fig. 5c draws a comparison of rate performances of both cells. As expected, ZnSe@Zn–KVOH harvests a capacity of 294.2, 259.2, 232.9, 193.4 and 155.1 mAh g^{-1} at 0.5, 1.0, 2.0, 5.0 and 10.0 A g^{-1}, respectively. When the current density returns to 0.5 A g^{-1}, the device still retains a capacity of 253.1 mAh g^{-1}. This readily outperforms the bare Zn–KVOH cell under identical conditions. Such outstanding reversibility and rate capability could be attributed to the inhibition of dendrite formation/side reactions and the maintenance of a homogeneous interface *via* the versatile ZnSe coating, which functions as a high-performance artificial SEI layer. Nyquist plots before and after cycling also reveal that the ZnSe@Zn–KVOH cell exhibits lower charge-transfer resistance and promoted ion diffusion kinetics in comparison with the Zn–KVOH counterpart (Fig. 5d). The long-term cyclic stability of both cells was further evaluated (Fig. 5e). As for ZnSe@Zn–KVOH full cell, it manages to deliver an initial capacity of 194.5 mAh g^{-1} and stabilizes at 163.9 mAh g^{-1} after 1000 cycles with a retention rate of 84% at 5.0 A g^{-1}. In contrast, the capacity of bare Zn–KVOH cell sharply drops to 47.2 mAh g^{-1} after 1000 cycles.

More impressively, ZnSe@Zn anode harnessing mechanical robustness and large-scale availability enlists the construction of flexible AZIB full cells (see methods) toward practical applications (Supplementary Fig. 22). Fig. 5f presents the GCD profiles of assembled flexible AZIB at 2.0 mA cm^{-2} under various bending angles of 0°, 90°, 135°, and 180°. Notably, 97.8% of the initial capacity could be retained upon bending at 180°, showing excellent mechanical flexibility. As a proof-of-concept demonstration, Fig. 5g displays digital photos of the working states of two flexible AZIBs in tandem configuration, enabling to continuously powering a light emitting diode (LED) indicator under different bending angles, showing its application prospect in wearable electronics. Taken together, these results corroborate that the ZnSe overlayers can effectively inhibit the parasitic reactions at the anode/electrolyte interface and guide uniform Zn deposition in favor of advanced stability of AZIB.

Discussion

In summary, we have developed a high-performance Zn anode *via in-situ* CVD coating of ZnSe overlayer harnessing high uniformity, thickness tailorability and scalability. Thus-designed ZnSe@Zn anode demonstrates a high Zn utilization of 99.2% and an elongated cycle life of 860 h during repetitive Zn plating/stripping. Even experiencing harsh conditions (10.0 mA cm^{-2}/10.0 mAh cm^{-2}), it can still sustain to operate as long as 260 h, outperforming the state-of-the-art anode counterparts. The protection mechanism of ZnSe overlayer has been systematically explored by a suite of experimental characterizations in harmonization with theoretical simulations. The optimized interfacial manipulation throughout such a ZnSe layer can help accelerate the kinetics of Zn^{2+} deposition by reducing de-solvation energy and restrict the 2D diffusion of Zn^{2+} *via* strong Zn affinity. Meanwhile, HER and other side reactions can be effectively handicapped. As a result, the ZnSe@Zn anode exhibits stable cycling capability, low voltage hysteresis as well as smooth dendrite-free surface. Encouragingly, assembled ZnSe@Zn – KVOH full cell delivers a remarkable cycling stability with a capacity retention of 84% after 1000 cycles. Our ZnSe@Zn anodes affording versatility and simplicity may greatly promote the industrialization of Zn-based energy storage systems.

Methods

Preparation of ZnSe-coated Zn foil (ZnSe@Zn)

The ZnSe overlayer was realized *via* an ambient pressure chemical vapor deposition process using tube furnace (Thermo Fisher Scientific). In brief, Zn foil (thickness: ~0.1 mm; length: ~20 cm; 99.99% purity; Alfa Aesar) and Se powders (~100 mg, 99.99%, Aladdin) were placed at the downstream and upstream position, respectively. The quartz tube was purged for 30 min using 540 sccm (standard cubic centimeters per minute) Ar gas. Afterwards, 50 sccm H_2/Ar mixture (10% H_2) was used as the carrier gas during growth and cooling. The quartz tube was heated to 300 ℃ in 15 min, and then cooled to room temperature under preset dwelling time. The surface of Zn foil turned into faint yellow due to the formation of ZnSe. Then the ZnSe coated Zn foil (ZnSe@Zn) was annealed at 325 ℃ for 30 min with 10 sccm H_2/Ar. Note that the ZnSe coated Ti foil was fabricated by a similar process as compared to that of ZnSe@Zn foil except that the Ti foil was placed on top of Zn foil and the tube furnace was kept at 320 ℃ for 1 h.

Preparation of KVOH

KVOH nanostructure was prepared by a modified hydrothermal method[38]. Typically, 0.364 g V_2O_5 (Energy Chemical, 99%) and 0.087 g K_2SO_4 (Macklin, 99.99%) were dissolved into 80 mL of DI water, followed by slow dripping of 2.0 mL 30% H_2O_2 into the solution under magnetic stirring. After continuous stirring for 30 min, the orange mixture was gradually transformed into a transparent red solution, which was then transferred into 100 mL Teflon autoclave under 120 ℃ for 6 h. Upon centrifugation, the precipitates were dried by a cryodesiccation process for 30 h to preserve the urchin-shaped morphology. Finally, light green colored $KV_{12}O_{30-y}{\cdot}nH_2O$ (KVOH) powders can be obtained.

The KVOH electrode was prepared by casting slurry onto a Ti mesh. The slurry was composed of active material KVOH, conductive carbon (Super P) and binder (PVDF) with a mass ratio of 7:2:1. The electrode was then dried in a vacuum oven under 80 ℃ for 12 h. The mass loading was adjusted to ~1.0 mg cm^{-2}.

Electrochemical tests

The Zn-Zn symmetric cell, Ti-Zn asymmetric cell and KVOH-Zn full-cell were fabricated based on CR2032 coin cell configuration. Prior to assembly, all the foils were cut into circle discs with a diameter of 13 mm. The cells were assembled at ambient conditions at room temperature. The electrodes were separated by glass fiber separators (Φ = 19 mm, Whatman). 2 M $ZnSO_4$ aqueous solution was used as the electrolyte.

The GCD cycling tests were carried out on the Neware battery-testing system. EIS, linear polarization, chronoamperogram and CV measurements of the batteries were recorded on electrochemical workstation (CHI660E, China). The linear polarization measurements were recorded in a three-electrode configuration, where bare Zn or ZnSe@Zn plate were used as the working electrode, Zn foil as the counter electrode, and saturated calomel (SCE) as the reference electrode, respectively. Moreover, the ZnSe@Zn and bare Zn electrodes were also assembled into transparent symmetric cells[34], followed by an *in-situ* optical observation to detect electrode evolution during continuous Zn plating/stripping process at a current density of 5.0 mA cm^{-2}.

HER tests were carried out using a three-electrode system controlled by an electrochemical workstation (CHI 760E, China). Graphite carbon and Ag/AgCl electrode (filled with saturated KCl) were used as counter electrode and reference electrode, respectively. The reference electrode (Ag/AgCl) calibration was performed in 0.1 M H_2SO_4 electrolyte with a Zn plate (1×1 cm^{-2}) serving as the working electrode. Prior to the test, the solution was bubbled with N_2 gas for 30 min to establish a N_2 saturation conditions. Linear sweep voltammetry (LSV) was conducted at a scan rate of 2 mV s^{-1}. All potentials measured were calibrated to reversible hydrogen electrode (RHE) using the following equation:

E (*vs.* RHE) = E (*vs.* Ag/AgCl) + 0.059 pH + 0.198.

Theoretical calculations

All computations were performed by spin-unrestricted density functional theory, carried out by Vienna *Ab-initio* Simulation Package[39] with projector augmented wave pseudopotential[40]. Electronic exchange-correlation interactions were described by GGA-PBE[41] functional with the Grimme's D3 dispersion correction[42]. The kinetic energy cutoff with plane wave was set to be 400 eV. First Brillouin zone integrations were sampled by the mesh size 5×5×1 for Zn (001) slab and 4×4×1 for ZnSe (111) slab. Zn (001) and ZnSe (111) slab with periodically repeating (3×3) and (2×2) unit cell by 4 layers was constructed for the Zn atom adsorption, respectively. The thickness of vacuum layer was set to 15 Å. The bottom layer was fixed to the bulk position. The other layers and adsorbed Zn atom were relaxed fully until the total energy was less than 10^{-5} eV and residual force per atom was lower than 0.02 eV/Å. The

adsorption energy was calculated by the formula: $E_{ads} = E_{total} - E_{slab} - E_{zn}$, where E_{total}, E_{slab} and E_{Zn} are the total energy with/without the adsorption of Zn atom and atomic energy of Zn, respectively.

Electric field simulation

A parallel plate capacitor model was used to simulate the electric field distribution at the interface between anode and electrolyte based on COMSOL Multiphysics software. In this simplified model, the length of two electrodes was 2 μm and the distance between them was 1 μm. The protuberances of bare Zn surface were represented by two cones. Hemisphere arrays were used to represent ZnSe nanoparticles. The sizes of Zn protuberances and ZnSe nanoparticles in simulations were based on the results of SEM characterizations. The ionic conductivity of $ZnSO_4$ was 5 S m^{-1}.[43] The experimental observed voltage hysteresis (with/without ZnSe overlayer) was set as cathodic potential, while the anodic potential is a constant of zero.

Declarations

Data availability

The data supporting the findings of this work are available within the article and its Supplementary Information files. All other relevant data supporting the findings of this study are available from the corresponding author on request.

Acknowledgment

This work was financially supported by the National Natural Science Foundation of China (51702225), the Natural Science Foundation of Jiangsu Province (BK20170336), Suzhou Science and Technology Project-Prospective Application Research Program (SYG202038) and the China Post-doctoral Foundation (Grant No. 7131705619). The authors also acknowledge support from the Suzhou Key Laboratory for Advanced Carbon Materials and Wearable Energy Technologies, Suzhou, China.

Author contributions

J.Y.S. designed the concept. X.Z.Y., C.L., R.H., B.Z.L. and M.L.W. prepared and characterized the ZnSe@Zn anode and KVOH cathode. X.Z.Y., C.L., Z.X.S., Y.H.W., S.L. and Y.W.S. performed the electrochemical test and explored the protective mechanism using *in-situ* and *ex-situ* characterization tools. Z.T.S. conducted the DFT calculation. S.Y. performed the COMSOL simulations. X.Z.Y., S.X.D. and J.Y.S. wrote the manuscript. All authors discussed the experimental and theoretical results and commented on the manuscript. All authors have approved to the final version of the manuscript.

Competing interests

The authors declare no competing interests.

References

1. Chao D, *et al.* Roadmap for advanced aqueous batteries: from design of materials to applications. *Sci. Adv.* **6**, eaba4098 (2020).
2. Zhang Q, Luan J, Tang Y, Ji X, Wang H. Interfacial Design of Dendrite-Free Zinc Anodes for Aqueous Zinc-Ion Batteries. *Angew. Chem. Int. Ed.* **59**, 13180–13191 (2020).
3. Tang B, Shan L, Liang S, Zhou J. Issues and opportunities facing aqueous zinc-ion batteries. *Energy Environ. Sci.* **12**, 3288–3304 (2019).
4. Li C, *et al.* Directly grown vertical graphene carpets as janus separators toward stabilized Zn metal anodes. *Adv. Mater.* **32**, 2003425 (2020).
5. Li H, *et al.* Advanced rechargeable zinc-based batteries: Recent progress and future perspectives. *Nano Energy* **62**, 550–587 (2019).
6. Blanc LE, Kundu D, Nazar LF. Scientific challenges for the implementation of Zn-ion batteries. *Joule* **4**, 771–799 (2020).
7. Yang Q, *et al.* Do zinc dendrites exist in neutral zinc batteries: a developed electrohealing strategy to in situ rescue in-service batteries. *Adv. Mater.* **31**, 1903778 (2019).
8. Yang Q, *et al.* Dendrites in Zn-based batteries. *Adv. Mater.* **32**, 2001854 (2020).
9. Cao Z, Zhuang P, Zhang X, Ye M, Shen J, Ajayan PM. Strategies for Dendrite-Free Anode in Aqueous Rechargeable Zinc Ion Batteries. *Adv. Energy Mater.* **10**, 2001599 (2020).
10. Ma L, *et al.* Toward practical high-areal-capacity aqueous zinc-metal batteries: quantifying hydrogen evolution and a solid-ion conductor for stable zinc anodes. *Adv. Mater.*, DOI: 10.1002/adma.202007406, (2021).
11. Yi Z, Chen G, Hou F, Wang L, Liang J. Strategies for the stabilization of Zn metal anodes for Zn-ion batteries. *Adv. Energy Mater.* **11**, 2003065 (2020).
12. Cao L, *et al.* Solvation structure design for aqueous Zn metal batteries. *J. Am. Chem. Soc.* **142**, 21404–21409 (2020).
13. Wang F, *et al.* Highly reversible zinc metal anode for aqueous batteries. *Nat. Mater.* **17**, 543–549 (2018).
14. Zhang N, *et al.* Cation-deficient spinel $ZnMn_2O_4$ cathode in $Zn(CF_3SO_3)_2$ electrolyte for rechargeable aqueous Zn-ion battery. *J. Am. Chem. Soc.* **138**, 12894–12901 (2016).
15. Zhang Q, *et al.* The three-dimensional dendrite-free zinc anode on a copper mesh with a zinc-oriented polyacrylamide electrolyte additive. *Angew. Chem. Int. Ed.* **58**, 15841–15847 (2019).
16. Zhang N, Huang S, Yuan Z, Zhu J, Zhao Z, Niu Z. Direct self-assembly of MXene on Zn anodes for dendrite-free aqueous zinc-ion batteries. *Angew. Chem. Int. Ed.* **60**, 2861–2865 (2020).
17. Zheng J, *et al.* Reversible epitaxial electrodeposition of metals in battery anodes. *Science* **366**, 645–648 (2019).

18. Han D, *et al.* A corrosion-resistant and dendrite-free zinc metal anode in aqueous systems. *Small* **16**, 2001736 (2020).
19. Cui M, *et al.* Quasi-isolated Au particles as heterogeneous seeds to guide uniform Zn deposition for aqueous zinc-ion batteries. *ACS Appl. Energy Mater.* **2**, 6490–6496 (2019).
20. Cai Z, *et al.* Chemically resistant Cu–Zn/Zn composite anode for long cycling aqueous batteries. *Energy Storage Mater.* **27**, 205–211 (2020).
21. Zhao K, *et al.* Ultrathin surface coating enables stabilized zinc metal anode. *Adv. Mater. Interfaces* **5**, 1800848 (2018).
22. Zhang Q, *et al.* Revealing the role of crystal orientation of protective layers for stable zinc anode. *Nat. Commun.* **11**, 3961 (2020).
23. Kang L, *et al.* Nanoporous $CaCO_3$ coatings enabled uniform Zn stripping/plating for long-life zinc rechargeable aqueous batteries. *Adv. Energy Mater.* **8**, 1801090 (2018).
24. Xie X, *et al.* Manipulating the ion-transfer kinetics and interface stability for high-performance zinc metal anodes. *Energy Environ. Sci.* **13**, 503–510 (2020).
25. Liang P, *et al.* Highly reversible Zn anode enabled by controllable formation of nucleation sites for Zn-based batteries. *Adv. Funct. Mater.* **30**, 1908528 (2020).
26. Hao J, *et al.* An in-depth study of Zn metal surface chemistry for advanced aqueous Zn-ion batteries. *Adv. Mater.* **32**, 2003021 (2020).
27. Deng C, *et al.* A sieve-functional and uniform-porous kaolin layer toward stable zinc metal anode. *Adv. Funct. Mater.* **30**, 2000599 (2020).
28. Cha E, *et al.* 2D MoS_2 as an efficient protective layer for lithium metal anodes in high-performance Li-S batteries. *Nat. Nanotechnol.* **13**, 337–344 (2018).
29. Xiang B, *et al.* Green-light-emitting ZnSe nanowires fabricated via vapor phase growth. *Appl. Phys. Lett.* **82**, 3330–3332 (2003).
30. Bai P, Li J, Brushett FR, Bazant MZ. Transition of lithium growth mechanisms in liquid electrolytes. *Energy Environ. Sci.* **9**, 3221–3229 (2016).
31. Guo W, *et al.* Dendrite-free Zn anode with dual channel 3D porous frameworks for rechargeable Zn batteries. *Energy Storage Mater.* **30**, 104–112 (2020).
32. Wood KN, *et al.* Dendrites and pits: untangling the complex behavior of lithium metal anodes through operando video microscopy. *ACS Cent. Sci.* **2**, 790–801 (2016).
33. Zhang K, Yan Z, Chen J. Electrodeposition accelerates metal-based batteries. *Joule* **4**, 10–11 (2020).
34. Zhao Z, *et al.* Long-life and deeply rechargeable aqueous Zn anodes enabled by a multifunctional brightener-inspired interphase. *Energy Environ. Sci.* **12**, 1938–1949 (2019).
35. Kundu D, Vajargah SH, Wan L, Adams B, Prendergast D, Nazar LF. Aqueous vs. nonaqueous Zn-ion batteries: consequences of the desolvation penalty at the interface. *Energy Environ. Sci.* **11**, 881–892 (2018).

36. Yan C, *et al.* Regulating the inner helmholtz plane for stable solid electrolyte interphase on lithium metal anodes. *J. Am. Chem. Soc.* **141**, 9422–9429 (2019).
37. Liang X, *et al.* A facile surface chemistry route to a stabilized lithium metal anode. *Nat. Energy* **2**, 17119 (2017).
38. Tian M, *et al.* Structural engineering of hydrated vanadium oxide cathode by K^+ incorporation for high-capacity and long-cycling aqueous zinc ion batteries. *Energy Storage Mater.* **29**, 9–16 (2020).
39. Kresse G, Furthmuller J. Efficiency of ab-initio total energy calculations for metals and semiconductors using a plane-wave basis set. *Comp. Mater. Sci.* **6**, 15–50 (1996).
40. Blochl PE. Projector augmented-wave method. *Phys. Rev. B* **50**, 17953–17979 (1994).
41. Perdew JP, Burke K, Ernzerhof M. Generalized gradient approximation made simple *Phys. Rev. Lett.* **78**, 1396–1396 (1997).
42. Grimme S, Antony J, Ehrlich S, Krieg H. A consistent and accurate ab initio parametrization of density functional dispersion correction (DFT-D) for the 94 elements H-Pu. *J. Chem. Phys.* **132**, 154104 (2010).
43. Rogac MB, Babic V, Perger TM, Neueder R, Barthel J. Conductometric study of ion association of divalent symmetric electrolytes: I. $CoSO_4$, $NiSO_4$,$CoSO_4$ and $ZnSO_4$ in water. *J. Mol. Liq.* **118**, 111–118 (2005).

Figures

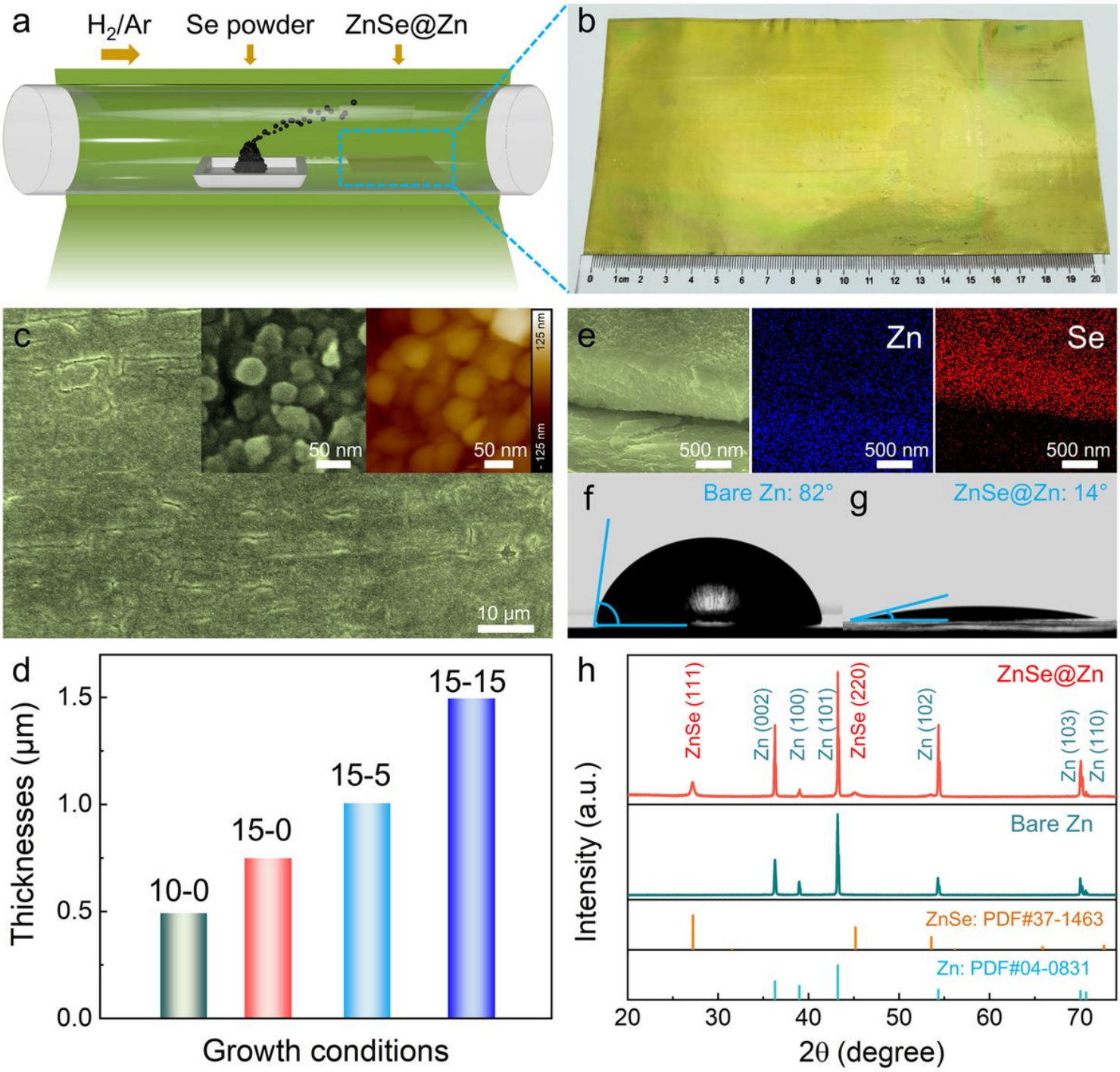

Figure 1

Synthesis and characterization of ZnSe@Zn. (a) Schematic illustration of CVD growth of uniform ZnSe overlayer on Zn foil. (b) Photograph showing a large-scale ZnSe@Zn product. (c) Top-view SEM image of ZnSe@Zn foil. Inset: High magnification SEM and AFM images of ZnSe@Zn. (d) Thickness histogram of ZnSe layer grown under different heating/dwelling time conditions. In this regard, “10-0” denotes that a heating time is 10 min and a dwelling time is 0 min. (e) Side-view SEM and elemental maps of ZnSe@Zn. Digital photo showing the contact angle values of ZnSO4 electrolyte on (f) bare Zn and (g) 0.75 μm-thick ZnSe@Zn. (h) XRD patterns of bare Zn and thus-prepared ZnSe@Zn.

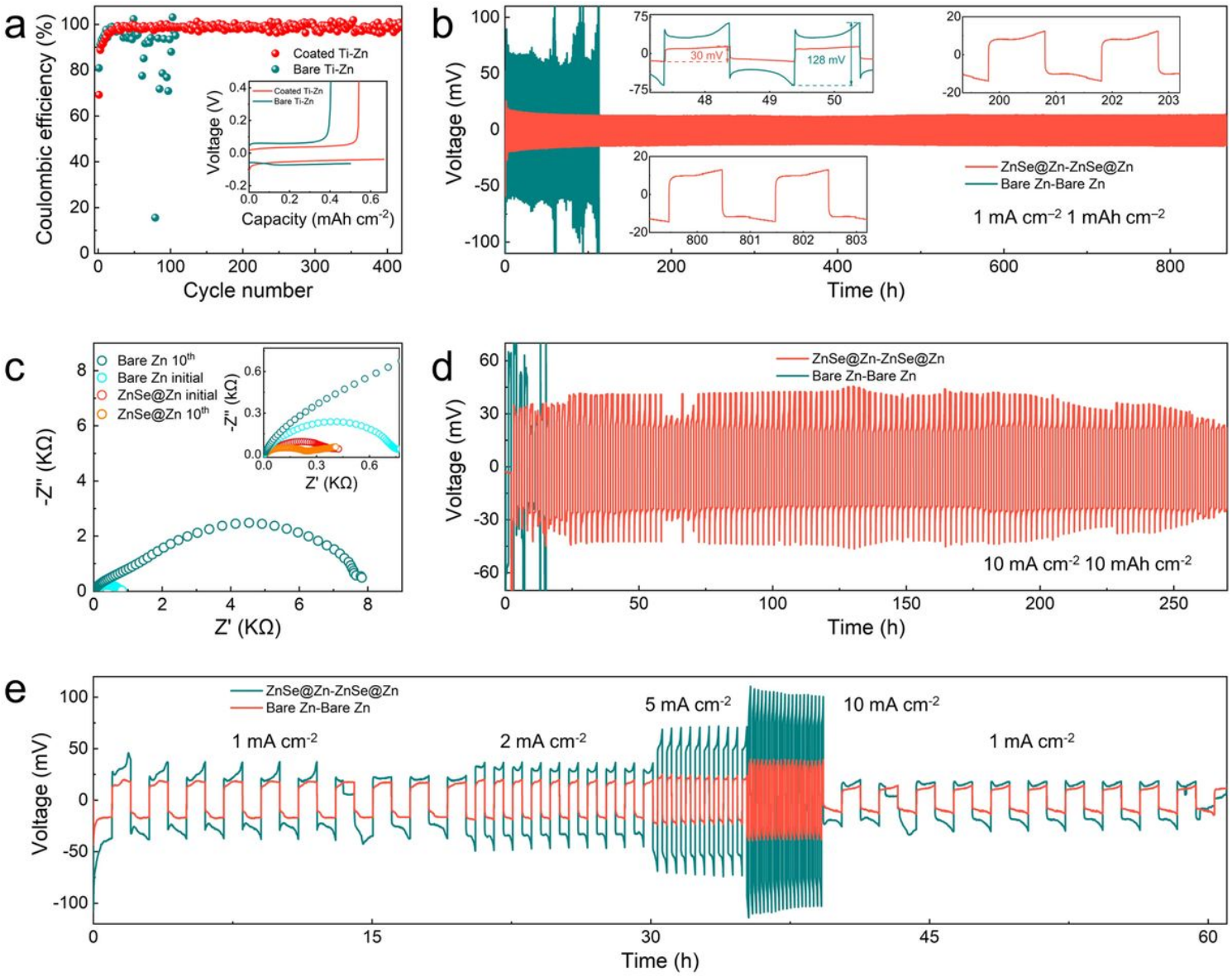

Figure 2

Electrochemical performances of the symmetric cells employing ZnSe@Zn and bare Zn electrodes. (a) Coulombic efficiencies of Zn plating/stripping process in ZnSe@Ti–Zn and bare Ti–Zn cells with a current density of 2.0 mA cm−2 and a capacity of 0.5 mAh cm−2. Inset: Corresponding voltage profiles at the first cycle. (b) Long-term galvanostatic cycling of ZnSe@Zn and bare Zn symmetric cells at a current density of 1.0 mA cm−2 and a capacity of 1.0 mAh cm−2. Inset: Detailed voltage profiles of ZnSe@Zn and bare Zn symmetric cells at specific cycling time. (c) Nyquist plots of symmetric cells using ZnSe@Zn and bare Zn before cycling and after 10 cycles. (d) Cycling performance of ZnSe@Zn and bare Zn symmetric cells at an elevated current density of 10.0 mA cm−2 and a capacity of 10.0 mAh cm−2. (e) Rate performances for ZnSe@Zn and bare Zn symmetric cells at various current densities with a capacity of 1.0 mAh cm−2.

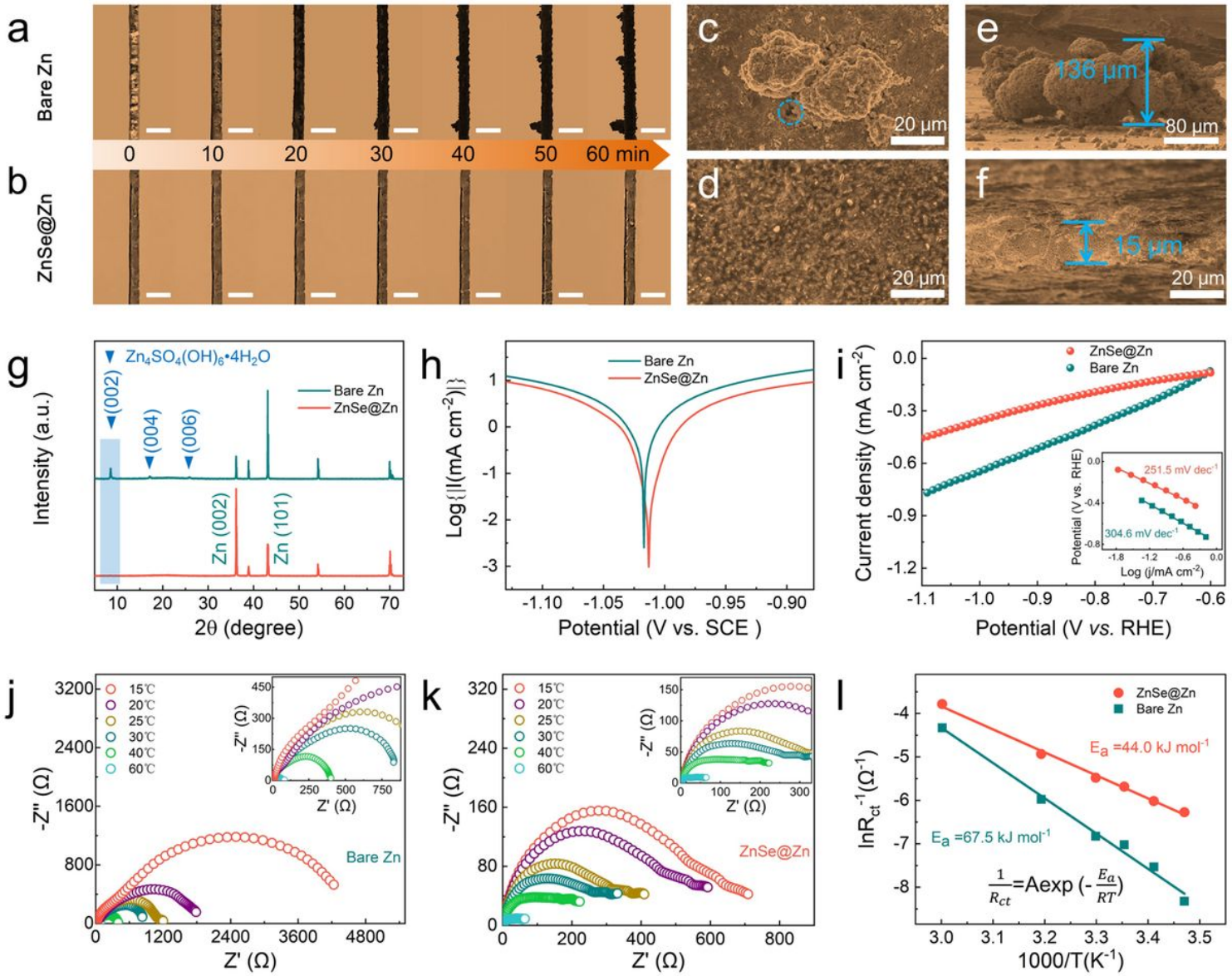

Figure 3

Instrumental insights into the protective effects of ZnSe overlayer on Zn anodes. In-situ optical microscopy visualization of Zn plating on (a) bare Zn and (b) ZnSe@Zn electrode at 5.0 mA cm−2. Scale bars: 200 μm. Top-view SEM images of (c) bare Zn and (d) ZnSe@Zn electrodes after 40 cycles. Cross-sectional SEM image of (e) bare Zn and (f) ZnSe@Zn electrodes after 40 cycles. (g) XRD patterns of bare Zn and ZnSe@Zn electrodes after 40 cycles. (h) Linear polarization curves presenting the corrosion on bare Zn and ZnSe@Zn. (i) Linear sweep voltammetry profiles of bare Zn and ZnSe@Zn. Inset: Tafel plots. Nyquist plots at different temperatures for (j) bare Zn and (k) ZnSe@Zn. (l) Corresponding Arrhenius curves and comparison of activation energies of bare Zn and ZnSe@Zn.

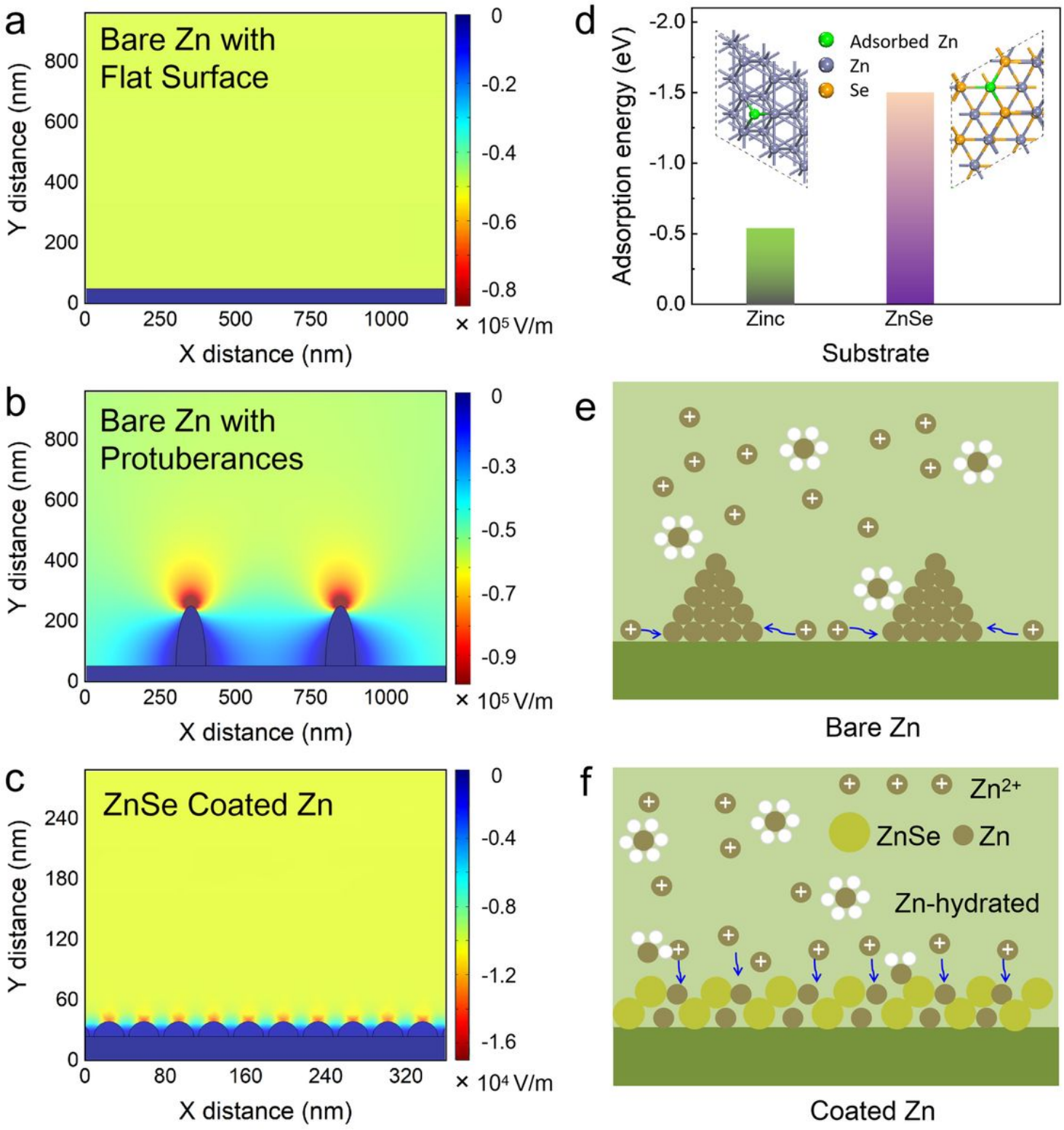

Figure 4

Theoretical simulation and analysis. Simulated electric field distributions on bare Zn electrode (a) without and (b) with protuberances. (c) Simulated electric field distributions on ZnSe@Zn electrode. (d) Adsorption energy of Zn atom on Zn and ZnSe substrates. The inset in (d) shows the corresponding computational models. The green, gray and orange ball represents the Zn adatom, Zn and Se atoms,

respectively. Schematics of Zn2+ diffusion and reduction processes on (e) bare Zn and (f) ZnSe@Zn electrodes, respectively.

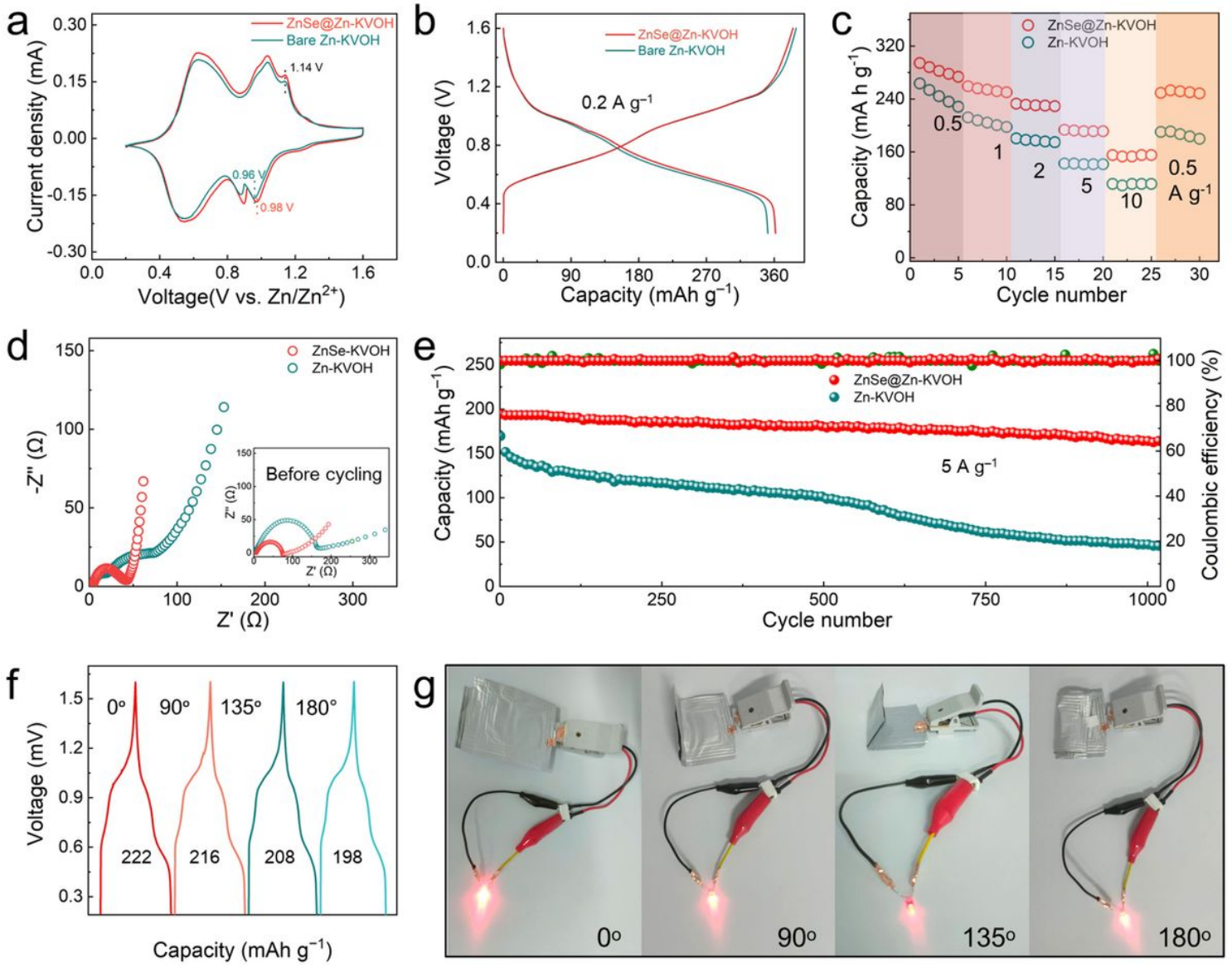

Figure 5

Electrochemical performances of Zn-KVOH full cells affording bare Zn or ZnSe@Zn anode. (a) CV curves at a scan rate of 0.1 mV s−1. (b) GCD profiles at 0.2 A g−1. (c) Rate performances. (d) Nyquist plots before and after cycling. (e) Long-term cycling performances at 5.0 A g−1 for 1000 cycles. (f) GCD profiles of a flexible ZnSe@Zn-KVOH cell tested at 2.0 mA cm−2 under different bending angles. (g) Digital photos showing the working states of flexible ZnSe@Zn-KVOH cells in series to power a LED indicator under different bending angles.

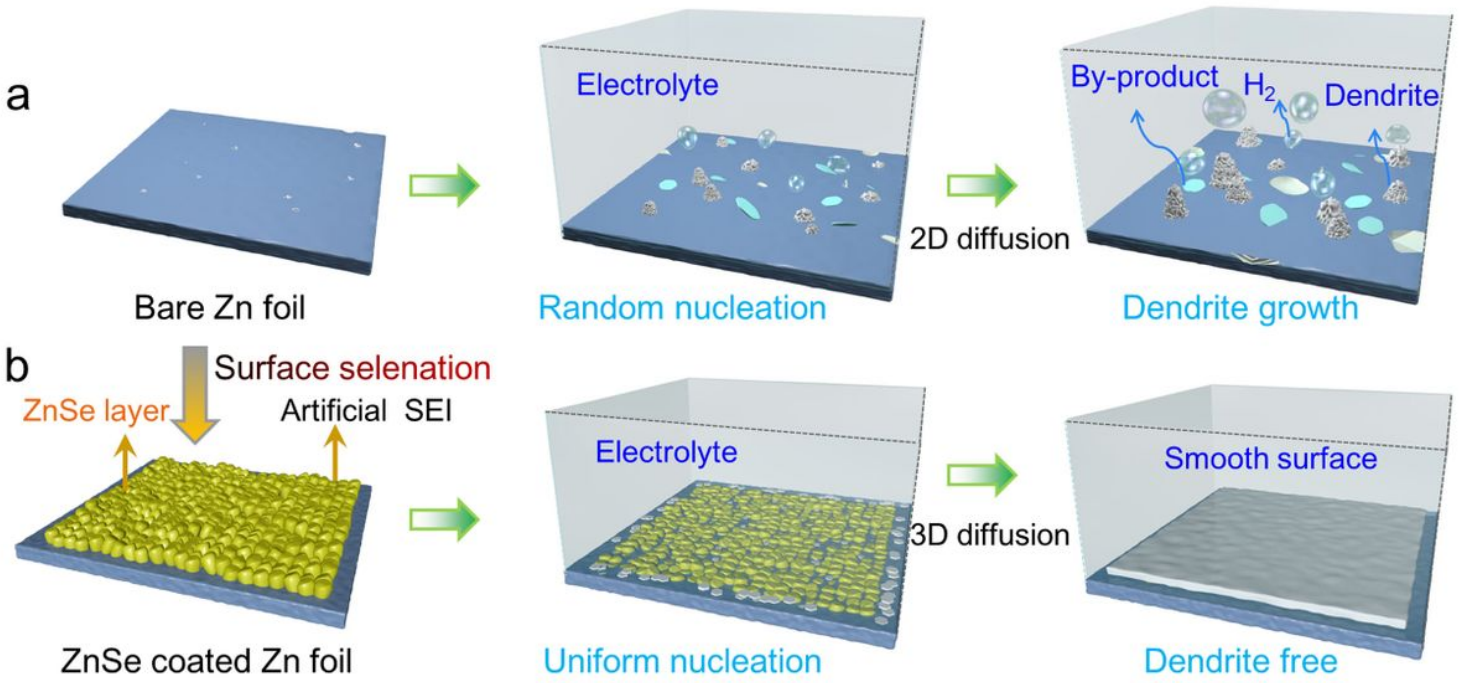

Figure 6

Scheme 1 Schematic diagram showing Zn deposition on bare Zn anode and ZnSe@Zn anode. (a) Severe corrosion, dendritic formation and hydrogen evolution occur on bare Zn anode upon electrochemical cycling. (b) Inhibited corrosion/hydrogen evolution and dendrite-free Zn deposition occur on ZnSe@Zn anode with in-situ grown ZnSe overlayer functioning as artificial SEI.

Supplementary Files

This is a list of supplementary files associated with this preprint. Click to download.

- ZnSeprotectedZnanodeSI2021.04.06.docx
- SupplementaryVideo1.mp4